

Optimization of solar water-heating combisystem deployed in an aquatic farm to mitigate hypothermia damage

Yueh-Heng Li*, Yu-Ting Yang

Department of Aeronautics and Astronautics, National Cheng Kung University, Tainan 701, Taiwan, ROC



HIGHLIGHTS

- Solar heating combisystem is to prevent hypothermia for aquatic farming.
- TRNSYS is to simulate solar combisystem under the required heating capacity.
- Taguchi method was used to optimize the geometry of the AF via STAR-CCM+.
- The survival zone of the AF's optimized geometry increased by 40%.
- Payback periods and CO₂ emission in three heating systems were determined.

ARTICLE INFO

Keywords:

Solar collector
Air-source HP
Combisystem
Aquatic farm
TRNSYS
Particle image velocimetry
STAR-CCM+
Taguchi method

ABSTRACT

In aquatic farms (AFs), renewable heating systems can aid in preventing hypothermia in aquatic creatures by maintaining an appropriate water temperature. However, heating and maintaining AFs at a certain water temperature during a cold stream event is difficult. As a technical and economical solution, a localized “survival zone,” with the appropriate water temperature, can be created in the water pool, where aquatic creatures can aggregate. Here, STAR-CCM+ was employed to simulate the three-dimensional temperature conditions of an AF in extreme weather and examine the survival zone volume. TRNSYS was used to simulate solar collectors (SCs) and a heat pump (HP) combisystem under the required heating capacity. The Taguchi method was used to optimize the geometry of the AF. In STAR-CCM+, eight parameters (distance between inlets 1 and 2, inlet heights, outlet positions, inlet velocity as fixed mass flow rate, barrier length, barrier position, barrier thickness, and barrier number) were compared. Of them, the two inlet heights, outlet positions, barrier length, and barrier position were selected according to their difference in percentage of the survival zone and set the orthogonal array for deployment in the Taguchi method. The survival zone of the AF's optimized geometry increased by 40%. In TRNSYS, three heating systems—namely boiler heating system, HP-boiler heating system, and SC-HP-boiler heating combisystem—were compared for their heating gain, contributions, payback period, and CO₂ emissions. Thus, solar combisystems effective in reducing CO₂ emissions are uneconomical and are not the most suitable heating system for cold streams. Nevertheless, boiler heating systems are potentially the most suitable for the optimized geometry of the AF during a cold current, particularly for instant heating.

1. Introduction

Taiwan (23°N, 120°E) has a tropical monsoon climate; however, strong cold streams occasionally hit the island during winter. In January 2016, a strong cold current hit Taiwan, which reduced the temperature to < 10 °C and caused unprecedented financial losses to the agriculture and fishery industries. According to Taiwan's Council of Agriculture, the economic losses reached approximately US\$100 million, constituting 54% of the total economic losses in Tainan in 2016. In

January 2018, another cold current caused approximately US\$15.95 million in economic losses, constituting approximately 84% of the economic losses in Tainan. Another cold current in February 2018 led to economic losses of 31.01 million, of which 21% was incurred in Kaohsiung.

Mixed cultivation of two species, such as milkfish (*Chanos chanos*) and whiteleg shrimp (*Litopenaeus vannamei*), may ensure remunerative profit. However, most fish and shrimp cannot tolerate low-temperature surroundings. Milkfish and shrimp tend to die when the surrounding

* Corresponding author.

E-mail address: yueheng@mail.ncku.edu.tw (Y.-H. Li).

<https://doi.org/10.1016/j.applthermaleng.2019.114863>

Received 2 September 2019; Received in revised form 23 December 2019; Accepted 27 December 2019

Available online 31 December 2019

1359-4311/ © 2019 Elsevier Ltd. All rights reserved.

Nomenclature			
A_{sc}	solar collector area [m ²]	S_{ω}	user-specified source terms [-]
a_0	intercept efficiency [-]	T	temperature [°C]
a_1	efficiency slope [-]	T_2	temperature at the solar collector inlet [°C]
a_2	efficiency curvature [-]	T_4	temperature at the solar collector outlet [°C]
\hat{a}	face area vector [m ²]	ΔT	temperature difference between solar collector inlet and ambient [°C]
F	flow rate [LPM]	l	characteristic length [m]
f_{β^*}	free-shear modification [-]	$Q_{SC,ex}$	collected solar thermal energy of the experiment [kJ/kg]
f_c	curvature correction [-]	$Q_{SC,si}$	collected solar thermal energy of the simulation [kJ/kg]
G	global irradiation [W/m ²]	Re	Reynolds number [-]
G_k	turbulent production [-]	V	cell volume [m ³]
G_{ω}	production of specific dissipation rate [-]	\hat{v}	velocity [m/s]
G_{nl}	non-linear production [-]	\hat{v}_g	grid velocity [m/s]
G_k^{lim}	additional production term to ensure proper generation of k at transition points [-]	<i>Greek symbols</i>	
I	turbulence intensity [-]	β^*	coefficient = 0.09 [-]
I_t	global radiation incident on the solar collector [W/m ²]	γ	coupling with transition model of the Gamma transition model [-]
k	turbulent kinetic energy [-]	μ_t	relation for turbulent viscosity [kg/m-s]
k_0	ambient turbulence values in source terms [-]	ρ	Density [kg/m ³]
P_{piezo}	Piezometric pressure [Pa]	$\sigma_k, \sigma_{\omega}$	inverse turbulent Schmidt numbers, $\sigma_k = 0.5$; $\sigma_{\omega} = 0.5$ [-]
P_{static}	static pressure [Pa]	μ	dynamic viscosity [kg/m-s]
S	mean Strain rate tensor [-]	ω_0	ambient turbulence values in source terms [-]
S_k	user-specified source terms [-]		

temperature decreases to < 10 °C and < 9 °C, respectively. Thus far, fishers have implemented several methods in a pool to prevent the water temperature from decreasing rapidly during a cold stream, such as building shelters at the north side of the aquatic farm (AF), avoiding stirring the water, feeding, changing freshwater, and turning on the waterwheel. Moreover, fishers heat the water by using electric heaters, boilers, or furnaces. However, these methods are environmentally unsustainable as they require burning of fossil fuel to operate. Moreover, electricity is generated by nuclear and fossil fuel power stations in Taiwan. This necessitates research for alternative energy [1–3] to reduce carbon dioxide emissions.

1.1. Solar combisystem

Taiwan receives abundant solar radiation: 1200–1700 kWh/m² annually [4] and up to 4.64 kWh/m² daily in Southern Taiwan [5]. Thus, it is an ideal region to implement solar thermal energy use. Moreover, according to the International Energy Agency (IEA) 2015 report, solar thermal energy in 2050 could provide one-sixth of global total energy use for heating and cooling. Solar energy is one of the most promising renewable energy sources because it is sustainable, does not cause pollution, and notably, is available universally. Chu and Cruickshank [6] demonstrated that solar thermal energy use could prevent 800 GW carbon dioxide emissions annually and mitigate conventional fossil fuel depletion and reduce greenhouse gas emissions. Emmi et al. [7] found that solar thermal energy is commonly used worldwide, such as in domestic heating and cooling.

Solar water heating system utilization is limited by low solar irradiance, leading to the integration of an auxiliary heating system. The most common auxiliary water heating system is an electric heater. A conventional solar heating system includes solar collectors (SCs) and an electric heater in a storage tank. However, although an electric heater has low power efficiency, its operating cost is considerably low. The boilers are typically run on fossil fuels. Despite its rapid heating capacity, burning fossil fuel as a heat source leads to a considerable amount of CO₂ emission, adversely affecting the environment. Nonetheless, the capital cost and installation cost of a ground heat pump (HP) are higher than those of other auxiliary water heating systems. Hence, integrating an air-source HP into a solar combisystem is a plausible solution to

solve the inadequate solar irradiance problem. Moreover, the use of an HP as auxiliary energy for a solar combisystem can achieve 70% energy savings compared with electrical resistance or a direct-fired heater [8].

Solar combisystems are connected either in parallel or in tandem [6]. In parallel, the SCs and HP heat water independently and then pump hot water into the storage tank. When the energy provided by the SC heating loop is insufficient, the HP heating loop may then take the lead by filling the storage tank with heated water in parallel with the SC loop. In terms of the contributions of this solar and HP system to successful market penetration, a parallel-mode solar combisystem has the advantage of being less complicated than serial systems in terms of hydraulic connections and system control [9,10]. Consequently, the parallel system may be more robust and reliable. In general, seasonal performance factor (SPF) [11] denotes the ratio of total thermal energy produced and total electrical energy consumed. The SPF of a parallel solar combisystem is better than a serial solar combisystem [9].

Notably, the lower the operating temperature and the lower the investment costs, the longer is the lifetime of the solar heating system [12]. Kaci et al. [12] conducted a simulation of a hybrid solar water heating system for an Olympic swimming pool in Dar El Beida (36.17°N, 3.25°E) by using the simulation software TRNSYS and found that green technology could prevent > 7000 kg equivalent of CO₂ emissions. In addition, heat losses may be reduced using a thermal cover. Chow et al. [13] also used TRNSYS to simulate indoor swimming pool water and space heating by using a solar-assisted HP system in Hong Kong (22.16°N, 114.09°E), a tropical region, and found that the global fractional energy-saving factor be as high as 79% in November, with an economic payback period of < 5 years. Dongellini et al. [14] evaluated a solar water heating system with different types of flat SCs for an outdoor swimming pool in Bologna, Italy (44.47°N, 11.43°E) and found that the heating capacity of outdoor swimming pools' evacuated and unglazed SCs were the most suitable typologies and that the minimum value of the acceptable pool water temperature strongly influenced SC size.

Nouanegue et al. [15] simulated outdoor swimming pools in cold weather in Mont Tremblant by using TRNSYS and described the energy balance equations and discussed energy-saving with pool-cover time. Hahne and Kubler [16] analyzed outdoor swimming pools heated by the solar combisystem in Stuttgart, Germany by examining the pool

temperature during the operation of the solar water heating system. The authors found that evaporative heat losses, contingent to the wind speed, accounted for > 60% of the total heat loss and that thermal conductive loss to the ground typically amounted to < 1% of overall energy losses and can be neglected. They concluded that the pool surface should be covered when the pool was out of service. Ruiz and Martínez [17] heated an open-air swimming pool by using a solar water heating system at Alicante, southeast of Spain. The temperature of an open-air swimming pool strongly depends on the wind speed over the water surface, which is associated with pool surroundings. The primary cause of energy loss of the swimming pool is evaporation.

1.2. Computational fluid dynamics simulation for swimming pool

To analyze the contribution of the parameters on the AF, computational fluid dynamics (CFD) software was employed. Anaëlle et al. [18] simulated a typical swimming pool with three injectors and two overflow channels on ANSYS FLUENT and analyzed the water of the velocity flow and path lines. Lewis et al. [19] performed small-scale experiments, scaled by Buckingham Pi Theorem: a dye test experiment, for investigating disinfectant distribution, and a bead test experiment, for examining surface water movement. The transient simulation was employed using ANSYS Fluent (version 12.0). Cloteaux et al. [20] investigated how swimming pool design affects hydraulics based on experimental and computational CFD. Roldan and Rico [21] simulated an open-air swimming pool in steady-state in Colombia by using COMSOL Multiphysics and compared three hot water deployments and analyzed that the effects of different deployments of hot water sinks and sources on the temperature distribution and time required for a pool temperature to reach the setting point.

The volume of the relatively warm water decreases when the warm water mixes with colder water. Hot water, issued to maintain the water temperature, is produced by the solar combisystem during the cold current. However, either high energy consumption or high energy dissipation in the cold current can lead to high investment costs. Therefore, optimization of the pool inlet-outlet position is important. The pool system must be optimized to maximize energy usage.

Gao et al. [22] investigated the mixing characteristics of hot water inside a storage tank with different inlet velocities of the supply of cold

water by using three-dimensional numerical modeling techniques. Asari et al. [23] examined the four heights of the inlets and outlets through simulation. Ievers and Lin [24] considered the effects of the tank height-to-diameter ratios, mass flow rate of inlets, and height distance of inlet and outlet. Lavan and Thompson [25] assessed different inlet locations, inlet mass flow rates, and inlet diameters, and various height-to-diameter ratios. Kenjo et al. [26] studied thermal stratification in the storage tank and discussed three inlet levels of the water into the mantle, namely high, middle, and low.

Moreover, a guiding wall (or barrier) is placed into the tank or pool to enhance the hydraulic or thermal efficiency. Stamou [27] improved the hydraulic efficiency of the tanks in the water supply network of the greater area of Athens: 18 cases, including 9 initial cases and 9 cases with guiding wall (modified cases), were simulated using ANSYS CFX. Numerous researchers have explored the application of a solar combi-system water heating system in a swimming pool. However, few have investigated the temperature of the open-air pool, particularly temperature distribution inside the pool.

1.3. Motivation, objectives, and methodology

The aim of this study was to reduce hypothermia damage in fisheries resulting from a cold stream. The aim of the heating system was to prevent the temperature of the water deviating from that required to sustain the living conditions of the farmed organisms, such as milkfish and whiteleg shrimp. During a cold current, the AF temperature gradually decreases, causing fishes and prawn to die of hypothermia. Therefore, a water heating system needs to be set up. Therefore, this study has two objectives: (1) generating a “survival zone” with temperature > 10.5 °C and (2) replacing nonrenewable energy with solar combisystems to reduce CO₂ emissions further.

Fig. 1 illustrates the current study process, which consisted of two parts: (1) AF optimization through simulation on the CFD software STAR-CCM+ and (2) heating system analysis through simulation on TRNSYS. TRNSYS was used to investigate the effect of hydraulic layout on the solar combisystem and analyze the transient and dynamic systems. This numerical software can design the simulation model for solar combisystem. TRNSYS and STAR-CCM+ simulations can together provide the parameters, mass flow rates, and temperatures of the

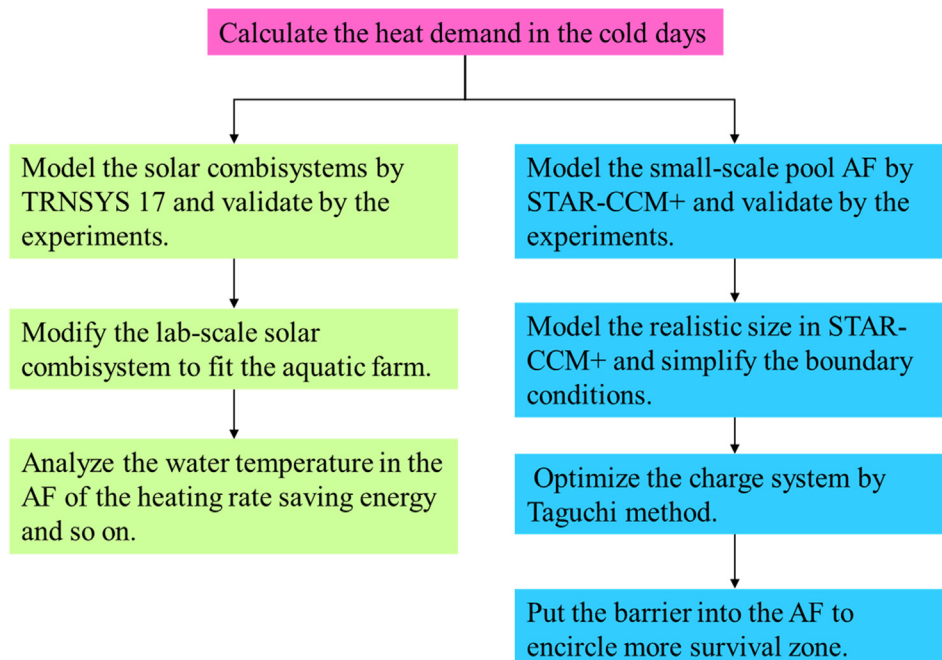


Fig. 1. Study process.

supplied hot water of a solar combisystem.

2. Scenario analysis of AF

This study assessed the improvement in the volume of the survival zone by using various water heating systems and floating barrier deployments. A survival zone was defined as an area where the water temperature was $> 10.5\text{ }^{\circ}\text{C}$, with even temperature distribution.

2.1. Geometry

In general, the area and depth of a deep AF should be $1250\text{--}7500\text{ m}^2$ and 2.0 m , respectively. Here, the dimensions of the aquatic pool were set to $50 \times 25 \times 2\text{ m}^3$ (length \times width \times depth), as shown in Fig. 2. The diameter of the hot water inlet and outlet tubes were fixed at 0.406 m . The point of origin ($x = 0, y = 0, z = 0$) was assumed to be fixed at the center point of the top rectangular surface; the inlets were at $(12.5, -0.5, -0.5)$ and $(12.5, -0.5, 0.5)$ and the outlets were at $(-1, -1.8, 25)$ and $(1, -1.8, 25)$.

2.2. Parameters of the material, physical model, boundary condition, and initial condition

In this study, the working fluid was water. Water density is the function of temperature. The physical 3D models incorporate the parameter setting of an unsteady state, gravity, and $\kappa\text{-}\omega$ turbulence, referred to Appendix A.

The following assumptions were made:

- A tent can be used as a shield on the top of the AF to alleviate heat loss from evaporation and forced convection.
- The mudstone temperature is affected by the ambient temperature and semi-infinite transient conduction; to simplify the wall boundaries, wall temperatures can be considered one-dimensional.
- The initial condition was the worst weather during the cold stream in January 2016 (Table 1).

The boundary condition was as follows in Appendix B. For inlets, the hot water was provided from the heating system. $20\text{ }^{\circ}\text{C}$ hot water was pumped at 25 kg/s via inlet tubes with a 406-mm diameter. The turbulence intensity (I) was determined as $I = 0.16(\text{Re})^{-1/8}$. For outlets, the water in the AF was discharged; the flow rate was similar to that of the inlets. The discharge system, inlets, and outlets were structured similar to a circulatory system, in that the input was the freshwater and the output the dirty water. For the sidewalls, the temperature increased with depth. The temperature of the floor was constant. On the surface, there was natural convection based on the aforementioned assumptions. The convection heat transfer coefficient described by Holman [28] was considered.

2.3. Grid test

The trimmed cell was applied using STAR-CCM+ due to the shape of the geometry. Some regions were refined mesh; for instance, the inlet-outlet flow regions were refined 50% and 25%; the regime in the vicinity of the sidewall was refined 50%. Table 2 displays the total number of cell elements under various conditions of cell size and mesh refinement. Fig. 3 presents the results of temperature contour at $x = 0\text{ m}$ in the $x\text{-}y$ plane for the grid test in the simulation after the hot water had entered for 30 min. Fig. 4 presents the numerical results of the grid test and the trend of the numerical results at $t = 30\text{ min}$. The temperature taken was that at the center of inlet 1 in the $x\text{-}y$ plane when hot water entered for 30 min. The error was calculated as (temperature in larger cell case-temperature in smallest cell case)/temperature in smallest cell case. For 0.5 and 0.3 cm/cell , the average error was 2.9% and 2.4%, respectively. Therefore, the 0.3 cm/cell was used

in this study.

2.4. Parameter analysis

Many parameters affected the water heating performance and the volume of the survival zone in the pool. To enlarge the survival zone, the barrier was used to deploy into the AF and encircle the warm water in a specific zone. The barrier material was polystyrene (PS), commonly used in beaches or jetties in Taiwan. The density, heat capacity, and thermal conductivity of PS were 1050 kg/m^3 , $1.3\text{ kJ/kg}\cdot\text{K}$, and $0.033\text{ W/m}\cdot\text{K}$, respectively.

The index was the difference between the percentages of the survival zone. This is defined as the difference in the percentages of the survival zone between two consecutive cases. It was used to indicate the performing capacity of the water heating system in two scenarios during the extremely cool stream.

The first parameter was the distance between inlets 1 and 2. Inlet 1 was fixed at $z = -0.5\text{ m}$, whereas the position of inlet 2 was changeable. In cases 1-1 and 1-2 (Fig. 5(a)), inlet 2 was positioned near the middle of the length and near the sidewall, respectively [$(x, y, z) = (12.5\text{ m}, -0.5\text{ m}, 0.5\text{ m})$ and $(12.5\text{ m}, -0.5\text{ m}, 0.5\text{ m})$, respectively]; moreover, in both these cases, the two outlets were positioned at $(x, y, z) = (12.5\text{ m}, -1.8\text{ m}, -24.5\text{ m})$ and $(12.5\text{ m}, -1.8\text{ m}, 23.5\text{ m})$.

The second parameter was inlet heights. The inlets were positioned at $y = -0.5\text{ m}$ near the water surface, whereas at $y = -1.5\text{ m}$ near the AF bottom. The buoyancy effect was focused on in these cases. In cases 2-1 and 2-2 (Fig. 5(b)), the inlets were positioned at $(x, y, z) = (12.5\text{ m}, -0.5\text{ m}, 0.5\text{ m}/-0.5\text{ m})$ and $(12.5\text{ m}, -1.5\text{ m}, 0.5\text{ m}/-0.5\text{ m})$, respectively, whereas the two outlets were positioned at $(x, y, z) = (12.5\text{ m}, -1.8\text{ m}, -24.5\text{ m})$ and $(12.5\text{ m}, -1.8\text{ m}, 23.5\text{ m})$.

The third parameter was different outlet positions. The positions of the inlets were fixed at $(x, y, z) = (12.5\text{ m}, -0.5\text{ m}, 0.5\text{ m}/-0.5\text{ m})$, and the positions of the outlets varied. In case 3-1 (Fig. 5(c)), the outlets were positioned at $(x, y, z) = (12.5\text{ m}, -1.8\text{ m}, -23.5\text{ m}/-24.5\text{ m})$ —same as the positions of the inlets, whereas in case 3-2, the outlets were positioned at $(x, y, z) = (-12.5\text{ m}, -1.8\text{ m}, -23.5\text{ m}/-24.5\text{ m})$, opposite to that of the inlets.

The fourth parameter was inlet velocity. The inlets and outlets were positioned at $(x, y, z) = (12.5\text{ m}, -0.5\text{ m}, 0.5\text{ m}/-0.5\text{ m})$ and $(12.5\text{ m}, -1.8\text{ m}, -23.5\text{ m}/-24.5\text{ m})$, respectively. The inlet velocity was changed by altering the diameter of the inlet in a fixed mass flow rate. In cases 4-1 and 4-2 (Fig. 5(d)), the radii were 0.1 and 0.2 m , respectively; other parameters are listed in Table 3. The Reynolds number (Re) was calculated based as

$$\text{Re} = \rho V D / \mu$$

and the turbulent intensity was calculated as

$$I = 0.16 \text{Re}^{-1/8}$$

The fifth parameter was barrier length. The presence of a barrier array in the AF was designed to enclose a warmer survival zone with identical water heating conditions. The barrier can defer the hot water entering the cool water zone through transverse diffusion. The barrier length and position therefore warrant further discussion. The barrier

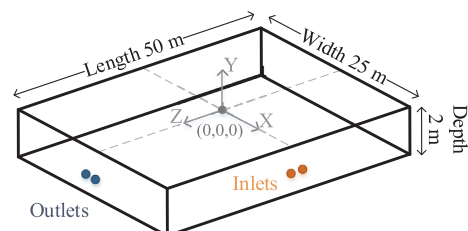


Fig. 2. Schematic of the AF with two inlets and two outlets.

Table 1
Weather conditions.

Observation time (LST)	Pressure of sea level (hPa)	Ambient temperature (°C)	Dew point temperature (°C)	Relative humidity (%)	Wind speed (m/s)
2016/1/25	1031.8	5.8	-0.5	63	8.2

Table 2
Example grid test.

Cell size (m)	Refined mesh (m)			Volume (m ³)	Cell elements
	50%	25%	10%		
0.4	0.2	0.1	0.04	2500	1,067,457
0.3	0.15	0.075	0.03		1,733,201
0.2	0.1	0.05	0.02		4,804,209

was placed into the AF at $x = 2.5$ m in the y - z plane. The top of the barrier was at $y = 0$ m, the same height as the water surface in the x - z plane, as shown in Fig. 5(e). Barrier lengths were 15 and 45 m in cases 5-1 and 5-2, respectively, and in both cases, barrier width and thickness were 0.2 and 1.5 m, respectively. The barrier was assumed to be composed of adiabatic material. In both cases 5-1 and 5-2, the inlet and outlet were positioned at $(x, y, z) = (12.5 \text{ m}, -0.5 \text{ m}, 0.5 \text{ m}/-0.5 \text{ m})$ and $(12.5 \text{ m}, -1.8 \text{ m}, -23.5 \text{ m}/-24.5 \text{ m})$, respectively.

The sixth parameter was the barrier position. In cases 6-1 and 6-2 (Fig. 5(f)), A 45-m-long barrier was placed at $x = 2.5$ and -7.5 m, respectively, with the distance from the inlet wall = 10 and 20 m, respectively. Inlets and outlets were fixed at $(x, y, z) = (12.5 \text{ m}, -0.5 \text{ m}, 0.5 \text{ m}/-0.5 \text{ m})$ and $(12.5 \text{ m}, -1.8 \text{ m}, -23.5 \text{ m}/-24.5 \text{ m})$, respectively.

The seventh parameter was barrier thickness, which plays a role in preventing hot water from undergoing thermal dissipation via thermal convection from the gap between the barrier and the bottom of the AF. In both cases 7-1 and 7-2 (Fig. 5(g)), a 45-m-long barrier was placed at $x = 2.5$ m, with barrier depth = 0.75 and 1.5 m, respectively. The manner in which hot water flows along the barrier and temperature distribution occurs in the pool was discussed. Inlets and outlets were fixed at $(x, y, z) = (12.5 \text{ m}, -0.5 \text{ m}, 0.5 \text{ m}/-0.5 \text{ m})$ and $(12.5 \text{ m}, -1.8 \text{ m}, -23.5 \text{ m}/-24.5 \text{ m})$, respectively.

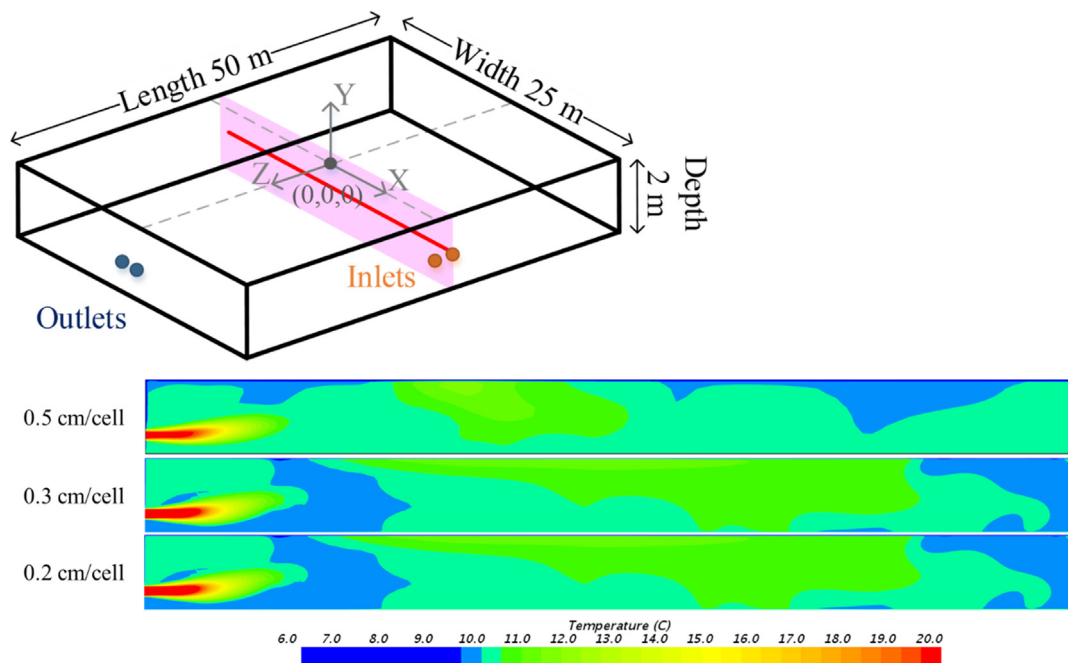


Fig. 3. Temperature contours at $x = 0$ m in the x - y plane in the grid test for simulation after hot water entered for 30 min.

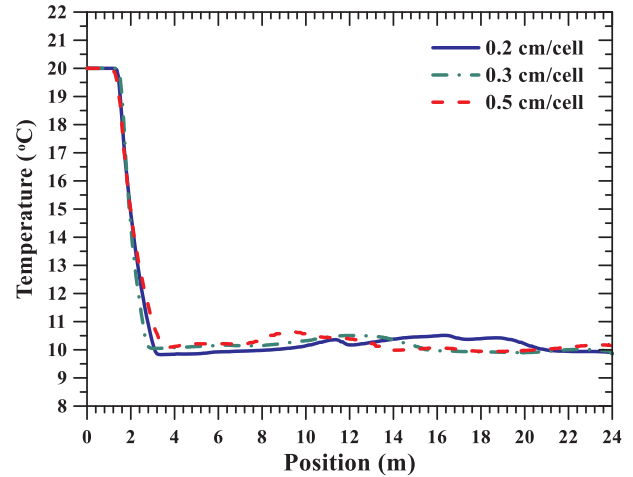


Fig. 4. Temperature and errors in the grid test at the inlet center of inlet 1 after hot water entered for 30 min.

$-1.8 \text{ m}, -23.5 \text{ m}/-24.5 \text{ m})$, respectively.

The eighth parameter was barrier numbers in a fixed barrier volume. A 30-m-long barrier was placed at $x = 2.5$ m in cases 8-1 and 8-2 (Fig. 5(h)); in both cases, overall barrier length was identical, but some barrier segments differed. In case 8-1, only one barrier was applied, whereas three barriers, with a segment length of 10 m and an inter-segment barrier gap of 0.2 m, were employed. The amount of hot water flowing across the gap and distribution of water temperature in the pool was discussed. Inlets and outlets were fixed at $(x, y, z) = (12.5 \text{ m}, -0.5 \text{ m}, 0.5 \text{ m}/-0.5 \text{ m})$ and $(12.5 \text{ m}, -1.8 \text{ m}, -23.5 \text{ m}/-24.5 \text{ m})$, respectively.

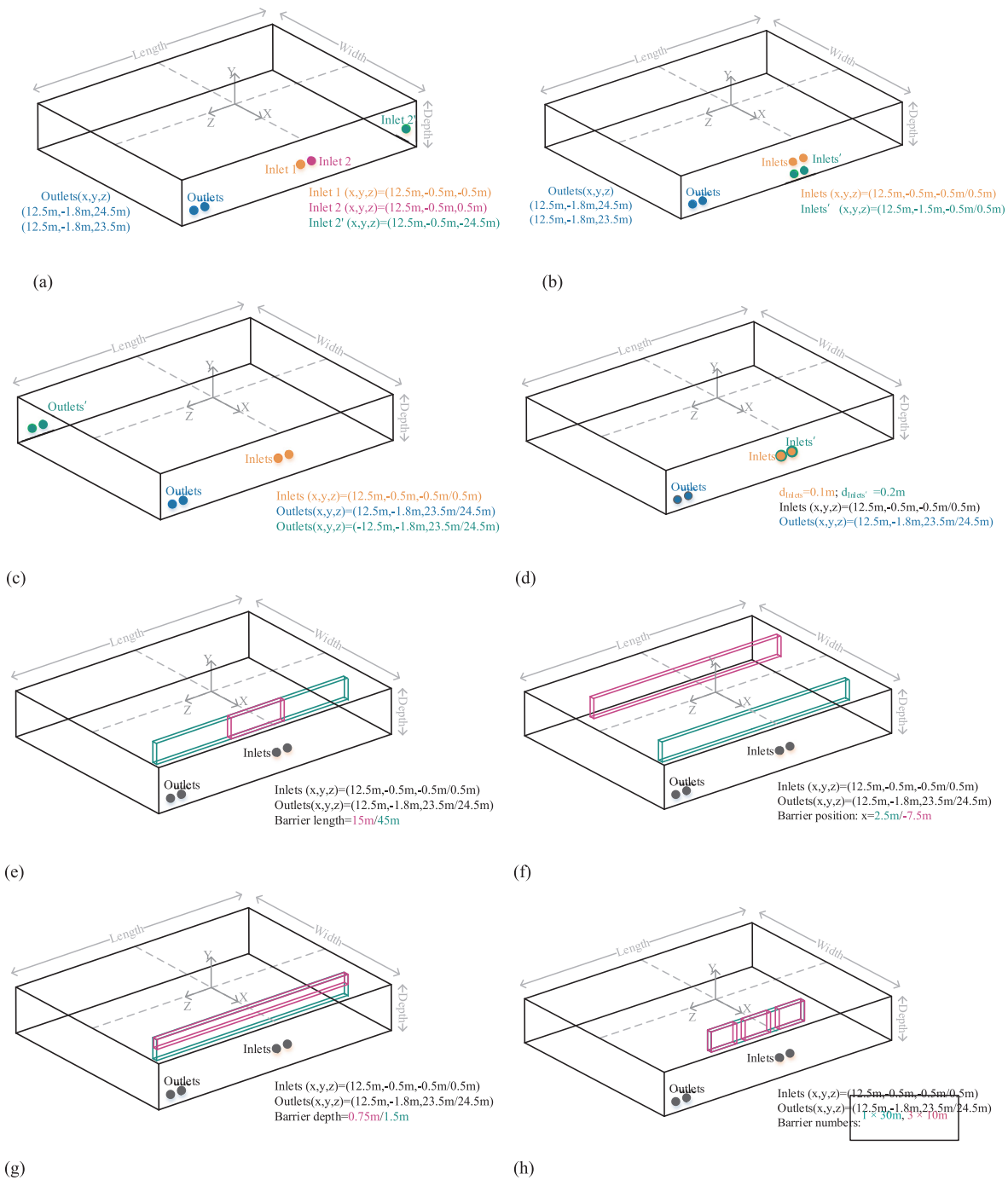


Fig. 5. Layout of inlets, outlets, and barriers in parameter analysis cases (a) 1-1 and 1-2, (b) 2-1 and 2-2, (c) 3-1 and 3-2, (d) 4-1 and 4-2, (e) 5-1 and 5-2, (f) 6-1 and 6-2, (g) 7-1 and 7-2, and (h) 8-1 and 8-2.

Table 3

Radius, velocity, Reynolds number (Re), and turbulent intensity (I) in cases 4-1 and 4-2.

Case	4-1	4-2
Radius (m)	0.1	0.2
Velocity (m/s)	0.80	0.20
Re (-)	159,159	79,580
I (-)	0.0358	0.0390

2.5. Optimizing the geometry of the AF using the Taguchi method

The results of the analysis of eight parameters are listed in Table 4. The parameters of outlet position, barrier length, and barrier position were selected owing to their significant difference in the percentage of survival zone > 10%. Inlet height was selected instead of the distance between inlets 1 and 2 because the inlet position was extremely close to the wall, as in case 1-2, which was not realistic. Furthermore, the hot water near the sidewall would enhance conductive heat loss. Moreover, the investment would increase when the distance between inlets 1 and 2 increases. Case 1-2 was neither realistic nor expensive, so inlet height replenished distance between inlets 1 and 2. As a result, four parameters were selected, inlet heights, outlet positions compared with inlet

Table 4
Parameter analysis results.

Case	Survival zone (m ³)	Percentage of survival zone (%)	Difference of percentage (%)
1-1	1936.18	77.73%	9.20%
1-2	1707.12	68.53%	
2-1	1936.18	77.73%	7.94%
2-2	2133.86	85.66%	
3-1	1936.18	77.73%	12.60%
3-2	1622.30	65.13%	
4-1	1709.80	68.64%	3.94%
4-2	1611.61	64.70%	
5-1	1273.12	51.03%	18.38%
5-2	811.85	32.65%	
6-1	1264.80	50.77%	14.47%
6-2	1625.18	65.24%	
7-1	1671.17	67.09%	0.47%
7-2	1682.76	67.55%	
8-1	1518.40	60.96%	0.98%
8-2	1494.07	59.98%	

positions, barrier length, and barrier position.

The Taguchi method was used to optimize the geometry of the AF and deployment of the barrier as well as the length of the barrier. The L9 (3⁴) orthogonal array refers to the orthogonal table, which was already set up, as shown in Table 5. In L9 (3⁴), “3” denotes the number of levels, with the three levels contained two limit values and one median value; “4” denotes the number of parameters, derived from the parameter analysis; and “9” denotes the total number of experiments. Based on four parameters with three levels, there were 81 experimental sets. Using the Taguchi method, the number of experimental sets reduces to nine. Table 6 presents the experimental numbers by L9 (3⁴) orthogonal array.

Table 7 presents the experimental results, including the survival zone and single-to-noise (S/N) ratio. The S/N ratio can normalize the index, survival zone. Here, the S/N ratio was based on the larger-the-better (LTB) formula. Table 8 presents each average S/N ratio and the difference between maximum and minimum. This difference can imply a degree of influence. The “barrier position” was sensitive to the geometry of the AF based on the highest difference between maximum and minimum; the “two heights of the inlets” had the least effect on this geometry. In Fig. 6, the maximum value of each parameter can be the best combination, which is (A3 B2 C2 D3). Its theoretical S/N ratio was 65.73 calculated using Eq. (1).

$$(S/N)_{opt} = (S/N)_{av} + (A3 - (S/N)_{av}) + (B2 - (S/N)_{av}) + (C2 - (S/N)_{av}) + (D3 - (S/N)_{av}) \quad (1)$$

where (S/N)_{av} is the total mean of the S/N ratio, whereas (S/N)_{opt} is the mean of the S/N ratio at the optimal level. A3, B2, C2, and D3 are maximum S/N response in four parameters, and the corresponding values are 64.07 for A3, 64.32 for B2, 64.54 for C2, and 64.76 for D3 (Table 8).

The final step of the Taguchi method was to validate the values and confirm the optimal conditions. From the value calculated via Eq. (1), the theoretical optimization value for the indicators was obtained (Table 9). To validate the accuracy of the Taguchi method, the best combination was simulated. The error of the S/N ratio was 0.80%, and the survival zone was calculated from the LTB formula. The errors of the percentage of survival zone were 6.18%, which is < 10% but acceptable.

3. Scenario analysis of the heating system

In this section, the assessment of the different heating systems of the AF during the cold current is reported. The heating performance of the various heating systems was simulated using TRNSYS. To validate the

accuracy of the simulation results, the laboratory-scale solar panel and HP combisystem was established, as shown in Fig. 7. After validating the parameter setting of each TRNSYS component, the heating capacity of the solar combisystem was enlarged to meet the heat demand of the AF during the cold current.

3.1. Validation of solar heating system

In this study, the laboratory-scale solar combisystem, which validates the simulation in TRNSYS, was established to provide hot water. The laboratory-scale solar combisystem was developed at the Guiren campus of National Cheng Kung University, Tainan, Taiwan. The laboratory-scale solar combisystem, which was controlled and monitored using LabVIEW, included four SCs, one HP, several thermal storage tanks (TSTs), water tanks, other pumps, and valves.

The laboratory-scale solar combisystem can perform three water heating system layouts. The first layout is a traditional solar hot water system (SHWS) composed of SCs and a TST. The second layout is an HP hot water system (HPHWS) composed of an HP and a TST. The third layout is an SC and HP combisystem composed of a combination of SCs and HP in parallel and a TST.

The SHWS is shown in Fig. 8. The water process in the SHWS is as follows: the water is pumped to the SCs, which heat the water through solar thermal heat; the hot water is delivered and stored in the storage tank. TST volume is 460 L. A flow meter was used to monitor the volume flow rate, which was fixed at 4.5 L/min by using valves. A pump was turned off when the temperature difference between SC inlet and outlet was < 3 °C and turned on when the temperature difference was > 7 °C.

The HPHWS is represented in case 2 (Fig. 9). The water process in the HPHWS is as follows: water is pumped to the HP from the TST; the HP heats the water; and finally, the hot water is delivered and stored in the TST. The TST volume was 460 L. A flow meter was used to monitor the volume flow rate, and the volumetric flow rate was fixed at 7.8 L/min by using a valve. The pump was controlled using LabVIEW according to the temperature and would turn off when the TST temperature achieved setting temperature and restart when the temperature difference was < 5 °C.

3.2. Validation of TRNSYS results – SHWS and HWS

Fig. 10 shows the numerical and experimental results for solar thermal energy by the SHWS system on a sunny spring day in March 2017. The SHWS system operated from 8:00 a.m. to 5:00 p.m. The initial TST temperature was 20 °C.

The solar thermal energy collected in the experiment, Q_{SC,ex}, was calculated using Eq. (2) (Fig. 7), whereas that collected in the simulation, Q_{SC,si}, was calculated using Eq. (3).

$$Q_{SC,ex} = F \times C_p \times (T_4 - T_2) \quad (2)$$

where F is the flow rate; C_p the specific heat capacity; and T_4 and T_2 the temperatures at the SC outlet and inlet, respectively.

$$Q_{SC,ex} = A_{SC} \times [a_0 I_t - a_1 \Delta T - a_2 (\Delta T)^2] \quad (3)$$

where A_{sc} is the SC area, a_0 the intercepted efficiency, I_t the global

Table 5
Four parameters with three levels in the Taguchi method.

Symbol	A	B	C	D				
Parameter	Two inlets of the height	Outlets position compared with inlets	Barrier length	Barrier position				
Unit	m	N/A	m	m				
Level 1	A1	0.5	B1	Neighboring	C1	15	D1	10
Level 2	A2	1.0	B2	Same	C2	30	D2	15
Level 3	A3	1.5	B3	Opposite	C3	45	D3	20

Table 6
Experimental number of L9 (3⁴) orthogonal array.

Symbol	A	B	C	D
Numerical no.	Two inlets of the height	Outlets position compared with inlets	Barrier length	Barrier position
Unit	m	N/A	M	m
1	0.5	Neighboring	15	10
2	0.5	Same	30	15
3	0.5	Opposite	45	20
4	1.0	Neighboring	30	20
5	1.0	Same	45	10
6	1.0	Opposite	15	15
7	1.5	Neighboring	45	15
8	1.5	Same	15	20
9	1.5	Opposite	30	10

Table 7
Cells, survival zone, percentage of survival zone, and S/N ratio of L9 (3⁴) orthogonal array.

Exp.	Cells	Survival zone	Percentage of survival zone	S/N Ratio
1	2,785,077	1469.36	0.59	63.34
2	2,638,082	1757.58	0.71	64.90
3	2,944,431	1576.86	0.63	63.96
4	2,638,082	1777.23	0.71	64.99
5	2,913,022	1369.07	0.55	62.73
6	2,946,478	1538.44	0.62	63.74
7	2,643,084	1495.30	0.60	63.49
8	3,077,696	1846.07	0.74	65.32
9	2,944,493	1535.33	0.62	63.72

radiation incident on the SC, a_1 the efficiency slope, a_2 the efficiency curvature, and ΔT the temperature difference between SC inlet and ambient.

As shown in Fig. 10, the trend of the numerical results was similar to that in the experimental results. The maximum average accuracy of the numerical results was 15%, and the minimum average accuracy of the numerical results error was 0%. The error of the SC thermal energy was caused by the difference in the flow rate because the flow rate of the simulation was the average flow rate of the experiments. Another error was derived from efficiency slope and efficiency curvature. The corresponding parameters of the SHWS system are listed in Table 10.

Fig. 11 shows the numerical and experimental results for the heat gained by the HP system on a sunny spring day in March 2017. The HPHWS system operated from 10:00 a.m. to 4:00 p.m. The initial temperature of the TST was 20 °C. The trend of the numerical results is similar to that of the experimental results. The maximum error was 4%. The reason for the different flow rates was that the flow rate of the simulation was the average flow rate of the experiment. This heat would dissipate to ambient, leading to the decrease in energy gained by the HP. The other parameters of the HPHWS are listed in Table 11.

3.3. Scenario heating system

The aim in TRNSYS was to prevent the water temperature of the AF from decreasing to < 15 °C because this would reduce the activity of

Table 8
Average S/N ratio of L9 (3⁴) orthogonal array.

Symbol	A		B		C		D					
Parameter	Two inlets of the height		Outlets position compared with inlets		Barrier length		Barrier position					
Unit	M		N/A		m		M					
Level 1	A1	0.5	64.07	B1	Neighboring	63.94	C1	15	64.14	D1	10	63.27
Level 2	A2	1.0	63.82	B2	Same	64.32	C2	30	64.54	D2	15	64.04
Level 3	A3	1.5	64.18	B3	Opposite	63.81	C3	45	63.39	D3	20	64.76
Max.- Min.			0.36			0.51			1.15			1.49

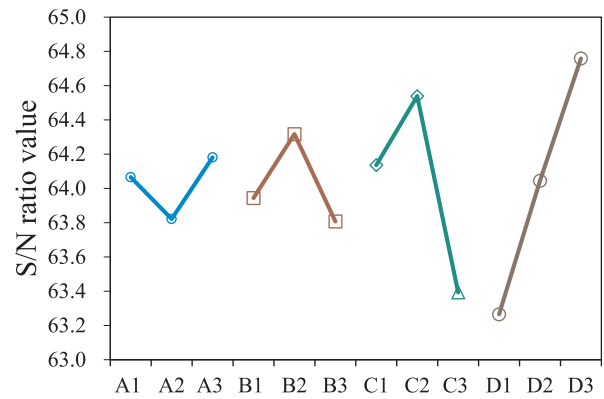


Fig. 6. S/N ratios for operational parameters.

Table 9
Comparison of predicted theoretical and experimental values from the Taguchi method.

	SN ratio	Survival zone	Percentage of survival zone
Theoretical	65.73	1933.66	77.6%
Simulation	65.21	1821.13	73.1%
Error	0.80%	6.18%	6.18%

the fish. Furthermore, a decrease in the water temperature of the AF to < 10 °C could lead to the death of the milkfish, particularly during the cold stream. The cold stream weather condition is illustrated in Fig. 12. This displays the weather conditions for 7 days including 3 normal days before a cold stream, 3 cold stream days, and 1 normal day after the cold stream. The ambient temperature was < 10 °C during the cold stream and the solar radiation was also lower than that on normal days, leading to the SCs not collecting sufficient solar radiation. Furthermore, the wind speed was higher than that on normal days and the convective heat loss increased during the cold stream. The heat collected from the environment was low, whereas the heat loss to the environment was high. Accordingly, integrating the water heating system to maintain water temperature to avoid hypothermia damage was necessary.

As shown in Fig. 12, the HP system and boiler system were turned on the day before the cold stream hit on January 22. This is because the Central Weather Bureau (CWB) typically issues a cold stream alarm the day before it arrives. The instant water heating system consequently becomes important and timely, such as in the HP system and boiler system. The solar thermal system was turned on in advance to store solar thermal in a TST. TSTs can be used as heat sources for the HP system. The overall heating schedule is displayed in Fig. 13. The HP system and boiler system were turned on from January 22 to 27. The solar thermal system ran throughout the January 20–27 period.

3.3.1. Heating system 1: Boiler heating system (B-System)

The boiler has been used as a conventional heating system thus far, the schematic of which is shown in Fig. 14. There are two closed loops in this system, HX-loop and boiler-loop, respectively. The HX-loop was

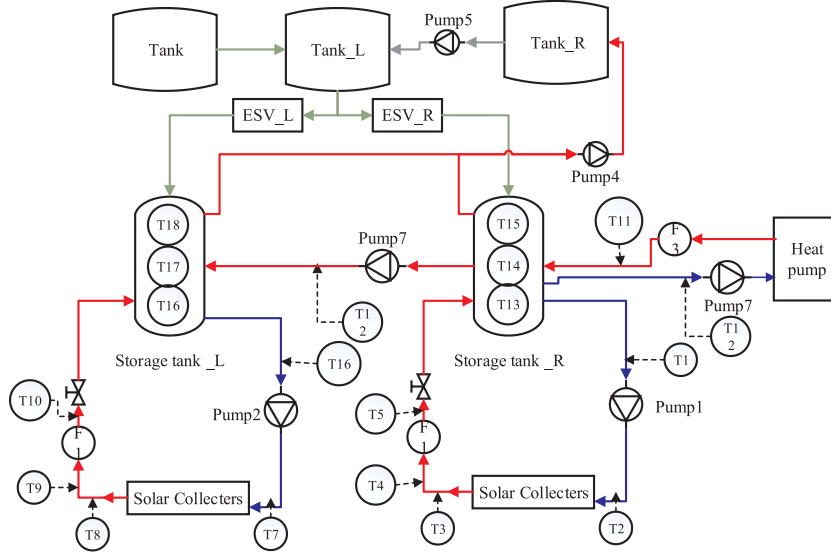


Fig. 7. Layout of the laboratory-scale solar panel and HP combisystem.

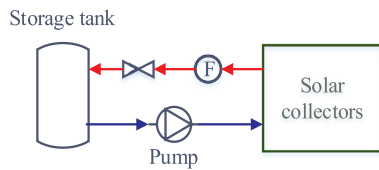


Fig. 8. Flow diagram of the SHWS.

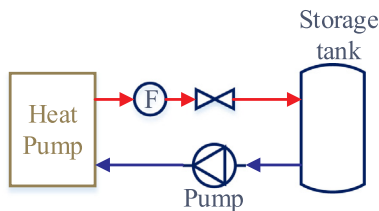


Fig. 9. Flow diagram of the HPHWS.

an in-directed heating method by HXs. The AF water was pumped to three HXs and then the heat in the HXs was extracted from the counterpart side of the HX and returned to the AF. This HX loop mimics the indirect heating process for the AF. The boiler-loop was charged to heat AF water, and the working fluid for this loop was water. The boiler-loop was turned on from January 22 to 27. The water was pumped to the boiler, and the boiler burned diesel oil and provided heat to the water in the loop. The hot water provided by the boiler was a heat source used by the HX to heat the AF water in the counterpart loop. The boiler was controlled by the temperature PID controller. This turned the boiler off when the water temperature of AF became $> 25\text{ }^{\circ}\text{C}$. This prevented the AF temperature from being higher than the living conditions and saves energy.

In TRNSYS, the weather data was provided by the TMY3 model and linked to the boiler, AF, and load side temperature of HX. The HXs (HX-1, HX-2, and HX-3 in Fig. 14) used were Type 5b, and the overall heat transfer coefficient was $28000\text{ kJ/kg}\cdot\text{K}$. The temperature and flow rate of the source side of HX opted to the boiler outlet temperature. The temperature of the load side of HX opted to the AF temperature, and the flow rate of the load side of HX was 25 kg/s at $20\text{ }^{\circ}\text{C}$. Type 659 was used as a boiler model, the rated capacity and flow rate of which were 290.7 kW and 6250 L/h , respectively. Type 2 was a temperature controller in the boiler-loop when the boiler system ran. Its setpoint temperature was $25\text{ }^{\circ}\text{C}$, which is the high limit for living conditions. Other parameter settings are listed in Table 12.

3.3.2. Heating system 2: HP and boiler heating system (HP-B-System)

The HP was involved in this system as it was an appropriate alternative to the solar thermal system, a renewable energy source, due to its high coefficient of performance (in short, COP of an HP is a ratio of useful heating provided to work required). The boiler-loop in this system was auxiliary energy, compensating for the lack of heat in HP. A schematic of the HP and boiler heating system (HP-B-System) is shown in Fig. 15. This system had three loops: HX-loop, boiler-loop, and HP-loop. The hydraulic parameters of the HX-loop and boiler-loop in the HP-B-System were identical to those of the boiler system. Characteristically, the heating capacity and flow rate of the boiler in HP-B-System were different from those of the boiler in the B-System. The heating capacity of the boiler in the HP-B-System was 162.8 kW , and the flow rate of the boiler was 3500 kg/h . The heating capacity of the boiler

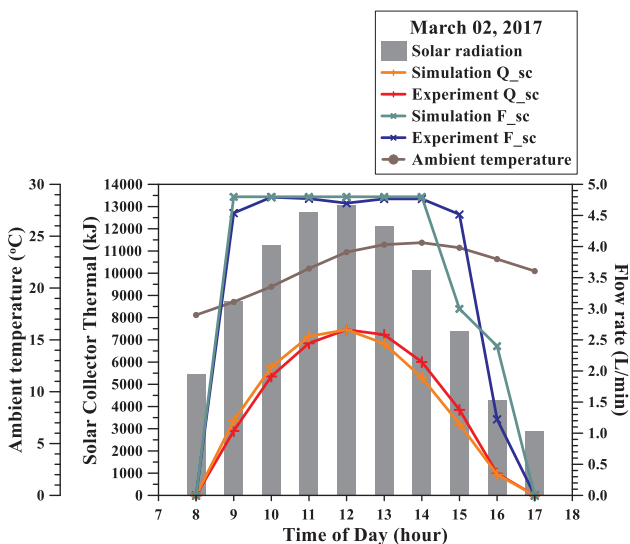


Fig. 10. Solar thermal energy collected and flow rates of SHWS from numerical simulation and experiment on a spring day.

Table 10
Parameter settings of validated SHWS model and experimental apparatus.

Parameters	Unit	Values
Solar collectors - Type1b		
Type	(N/A)	Flat plate
Collectors area	(m ²)	3.84
Intercept efficiency	(N/A)	0.645
Efficiency slop	(kJ/h-m ² -K ¹)	6
Efficiency curvature	(kJ/h ¹ -m ² -K ²)	0.02
1st-order IAM	(N/A)	0.42
Storage tank - Type4a		
Tank volume	(m ³)	0.46
Number of nodes	(N/A)	3
Material	(N/A)	304 stainless steel
Pump - Type3d		
Maximum flow rate	(kg/h)	288
Maximum power	(kW)	0.37
Temperature controller of the solar collector loop - Type2b		
Upper dead band dT	(°C)	7
Lower dead band dT	(°C)	3

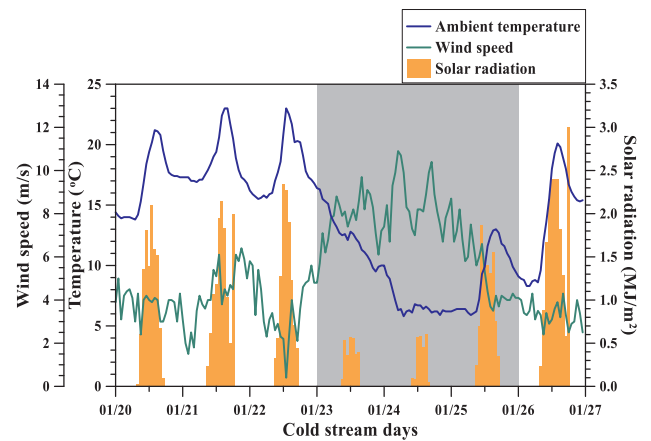


Fig. 12. Weather conditions from January 20 to 27, 2016.

there were 20 units of 2-t HPs because the heating capacity of 2-t HP was validated. According to the engineer's experience in R&G Service Energy Co. in Taiwan, the heating capacity of 10 units of 2-t HPs is equivalent to 1 unit of 20-t HP. Therefore, 20 units of 2-t HPs are equivalent to 2 units of 20-t HPs. The working fluid in the HP-loop was water. When the HP system was turned on by Type 516, the water was pumped to the HP to receive the heat, which was given to the load side of the HXs (namely heating the water of AF), and then, returned to the HP. The parameter settings of 2-t HP are shown in Table 11.

3.3.3. Heating system 3: Combination of SC, HP, and boiler heating system (SC-HP-B-System)

The solar thermal system is considered a source of renewable energy in this system. The contribution of solar thermal energy to the water heating system of AF is low owing to cloudy or rainy days during the cold stream. Accordingly, a TST is necessary to store the heat from SCs. Fig. 16 illustrates a schematic of this combined SC, HP, and boiler heating system (SC-HP-B-System). In this system, there are four loops: HX-loop, boiler-loop, HP-loop, and solar-loop. The hydraulic parameters of the HX-loop, boiler-loop, and HP-loop in the SC-HP-B-System are identical to those in the HP-B-System. However, in the boiler-loop, the heating capacity and flow rate of the boiler are different. The 162.8- and 37.2-kW heating capacity of the boiler was employed in the SC-HP-B-System, with flow rates of 3500 and 800 kg/h, respectively.

The solar-loop was connected to an HP-loop and TST in tandem. In the solar-loop, the water was pumped to the SCs from the TST, heated in the pipe of the SCs, and drained back to TST. The water in TST then entered the HP-loop for further heating and drained back to TST. In solar loops, the SC area was 230.4 m², consisting of 120 panels of SCs, which was a maximum land area surrounded by the peripheral road of the AF. A flow rate of 0.4 kg/s was presumably provided for the system assembled with six SCs connected in tandem and a 1-t TST. Therefore, the flow rate of this combisystem should have been 8 kg/s, and the volume of TSTs should have been 20 t. In the solar-loop, the PID controller was employed to control the operation of the solar-loop by monitoring the water temperature of TST. The initial temperature of TST was 24 °C and the heat loss coefficient was 3 W/m²-K in TRNSYS. Other parameters are listed in Table 13.

3.4. System comparisons

3.4.1. AF temperature

Fig. 17 shows the average water temperature of AF and heat loss from the AF to the environment. The temperature of the AF without a heating system, labeled as T-AF-0, changed with the ambient temperature, T-amb (Fig. 17). There is a time delay on the AF temperature due to thermal conduction and there is less temperature oscillation in

Fig. 11. HP thermal energy collected and flow rates of HPHWS from numerical simulation and experiment on a spring day.

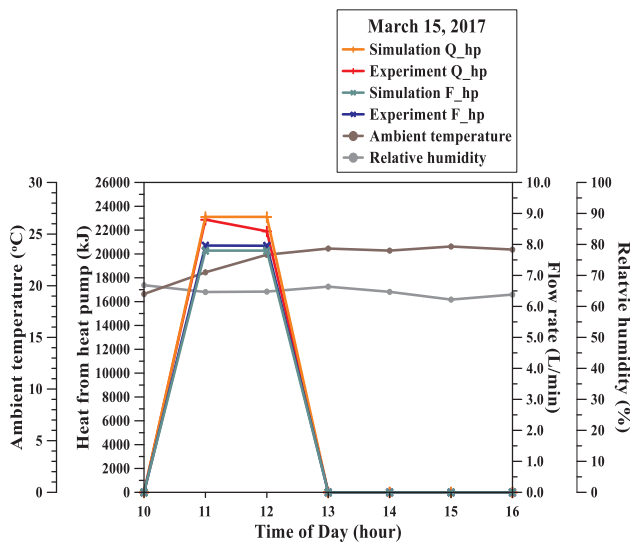


Table 11
Parameter settings of validated HPHWS model and experimental apparatus.

Parameters	Unit	Values
HP - Type938		
Refrigerant	(N/A)	R410A
Rated compressor power	(kW)	1.7
Rated heat capacity	(kW)	7
Total air flow rate	(L/s)	717
Blower power	(kJ/h)	662
Temperature controller of HP loop - Type2		
Set point temperature	(°C)	55
High limit monitoring temperature	(°C)	
Turn on temperature difference	(°C)	5
Turn off temperature difference	(°C)	0
Storage tank - Type4a		
Tank volume	(m ³)	0.46
Number of nodes	(N/A)	3
Material	(N/A)	304 stainless steel

decreases because the system has other heating components, such as HPs.

The HP-loop provides heat through another method. In this system,

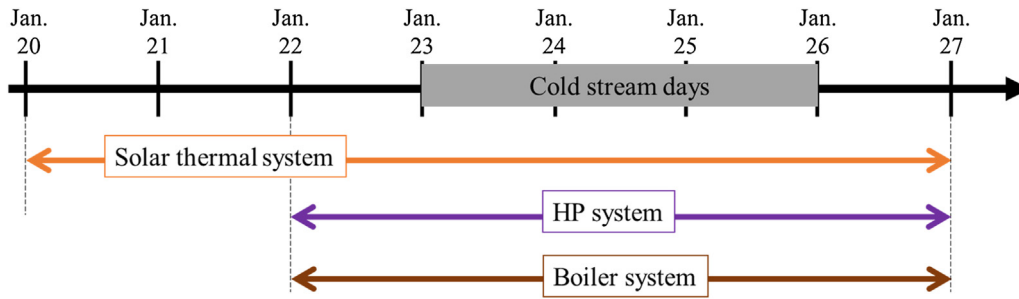


Fig. 13. Heating schedule of solar heating combisystem.

the AF, compared with ambient temperature, due to specific heat. The ambient temperature, T_{amb} , can be $> 15\text{ }^{\circ}\text{C}$ before the cold stream, from January 20 to 22. The T_{AF-0} was also $> 15\text{ }^{\circ}\text{C}$, indicating that the farmed organisms all survived. When the cold stream hit Taiwan on January 23, the T_{amb} rapidly decreased to approximately $6\text{ }^{\circ}\text{C}$ on January 20, a low temperature that lasted for 2 days. The ambient temperature began to increase again at noon on January 25, returning to the normal temperature on January 26. The T_{AF-0} decreased to nearly $7\text{ }^{\circ}\text{C}$ from January 23 to the noon of January 25. A study [29] reported that milkfish definitely dies when the water temperature decreases to $< 13\text{ }^{\circ}\text{C}$. Therefore, without a heating system, the farmed organisms, namely milkfish and whiteleg shrimp, would all have died. With the heating systems, the AF temperature would remain $> 15\text{ }^{\circ}\text{C}$ and all farmed organisms would survive.

In the boiler heating system, the AF average temperature, T_{AF-1} , is shown using a purple line in Fig. 17. The T_{AF-1} increased slightly until the boiler heating system turned on. The heat loss from the AF to the environment was negative because the ambient temperature was higher than the AF temperature; the AF thus received heat from the ambient. The T_{AF-1} increased when the boiler heating system, with 290.7-kW heating-capacity boilers, turned on. On January 22, the T_{AF-1} increased to $17\text{ }^{\circ}\text{C}$. However, during the cold stream, the high wind speed caused a high forced convection heat loss, which was greater than the heat gained from the boiler system. The T_{AF-1} maintained a temperature of approximately $15\text{ }^{\circ}\text{C}$ under energy balance. The T_{AF-1} increased until the day after the cold stream event ended. In an HP-B-System, the AF average temperature is similar to that of the T_{AF-1} because both heating systems have similar heating capacities. The total heat gained is indicated in Table 14.

In the SC-HP-B-System, the AF average temperature, $T_{AF-3-162B}$ and T_{AF-37B} , increased from January 20 due to the contribution of a solar-loop. The heat gained from the solar-loop can be noted in the days before the cold stream period (Fig. 18). The solar thermal energy was stored in TST and the heat was used to heat the AF water via HXs. Thus, the increase in AF temperature in the B-System is much more obvious than that in the HP-B-System. The AF temperature reached approximately $21\text{ }^{\circ}\text{C}$ at midnight on January 23, before the cold stream event. However, the greater the amount of heat gained from water heating systems, the greater was the amount of heat loss to the surroundings, as shown in Fig. 18. The heat loss increased during the cold stream event, causing a higher AF temperature slope. After the cold stream event, the AF temperature increased because the solar thermal system can extract solar radiation, as shown in Figs. 12 and 18.

In the aforementioned four systems, the average AF temperatures were all $> 15\text{ }^{\circ}\text{C}$. Consequently, all farm organisms would have been

Table 12

Parameter settings of the boiler heating system.

Parameters	Unit	Value
Boiler - Type 659		
Rated capacity	kW	290.7
Pump	liter/h	6250
Consumption power	kg/h	3708
Temperature controller - Type2		
Set point temperature	$^{\circ}\text{C}$	25
High limit monitoring temperature	$^{\circ}\text{C}$	70
Turn on temperature difference	$^{\circ}\text{C}$	2
Turn off temperature difference	$^{\circ}\text{C}$	0
Heat exchanger (HX) extract heat - Type 5b		
Overall heat transfer coefficient of an exchanger	$\text{kJ/kg}\cdot\text{K}$	280,000
Total load side flow rate	kg/s	25

able to survive the cold stream.

3.4.2. Proportion of heat source

The HP, SCs, and thermal storage were used in this study as a substitute for the conventional fossil fuel-burned heating system. The proportion of heat gained from each system was examined to reduce fossil fuel dependency and achieve carbon abatement. Table 14 lists the contributing proportion of each heating system. For the B-System, only a boiler can provide the heat. Therefore, the proportion of the boiler in the B-System is 100%. The proportionate heat gain from the HP-B-System was 44% in HP and 56% in the boiler; the heat gain from the SC-HP-B-System in a 162.8-kW heating-capacity boiler was 56% in the boiler and 44% in the others. The reason for the proportion of the boiler being greater is related to the flow rate of the source side of the HX, which limits heat absorbency. The heat gain from the SC-HP-B-System in a 37.2-kW heating-capacity boiler was 22% in the boiler and 78% in others. This was due to the low heating capacity of the boiler.

3.4.3. Economic assessment

An economic assessment is essential because affordability is strongly related to the willingness to install a solar combisystem. The total, investment, and operating costs were all considered. Information in the investment cost in the solar thermal system and HP system was provided by R&G Service Energy Co. The 120-plate SCs cost NT\$1,000,000, a 20-t HP costs NT\$300,000, a 20-t TST costs NT\$200,000, a circulation motor costs NT\$10,000, and system installation fee is NT\$200,000. Moreover, R&G Service Energy Co. and Taiwan Masahisa Machinery Co. provided investment cost information for the boiler system. A 37.2-, 162.8-, and 290.7-kW heating-capacity boiler costs NT\$150,000,

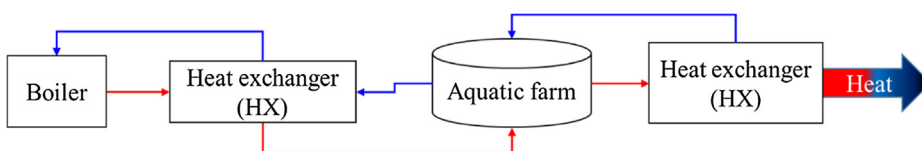


Fig. 14. Schematic of the layout of the TRNSYS of boiler heating system.

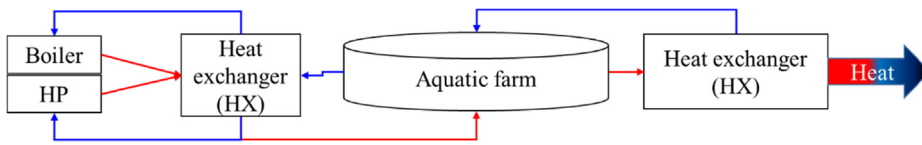


Fig. 15. Schematic of the layout of the TRNSYS of HP-B-System.

NT\$300,000, and NT\$450,000, respectively.

Fishers typically cultivate over 2–3 seasons in annually, and 1-ha deep-water culture can hold 22,000 milkfish and 1,050,000 whiteleg shrimp, at a cultivation cost of NT\$46.05/kg and NT\$17.87/kg, respectively. Moreover, 300 g of milkfish and 50 g of white leg shrimp can be sold at approximately NT\$13.815 and NT\$0.8935, respectively. Therefore, 0.125-ha AF can hold 2,750 milkfish and 13,125,000 whiteleg shrimp, equivalent to total revenue of NT\$155,263.

The weather data for the past 4 years (2015 – 2018) was collected from CWB Observation Data Inquiry System. The data demonstrate the days on which average daily temperature for 2 more days was < 15 °C, which occurs in January and February. These months are assumed to be in the same season; therefore, the fisher loses one season’s profit, NT\$155,263, in 1 year. If the fisher installs the aforementioned heating system, they can be exempted from the loss of one season’s profit. The parameter cost recovering time (in years) is defined a ratio of the total cost to the loss of 1 year, where the total cost is the sum of the investment and operating costs. The cost recovering time of each heating system is shown in Table 14.

The payback periods of B-System and HP-B-System are < 5 years, whereas that of two SC-HP-B-Systems is > 10 years. This is because the SC-HP-B-Systems included SCs and a 20-t TST. The proportion of the investment cost of the solar-loop is > 50%; however, the proportion of heat gain in each heating system is very low. Finally, the solar-loop is quiet and unsuitable for preventing hypothermia damage during the cold stream. The B-System has the lowest cost as well as the lowest payback period among all the heating systems.

3.4.4. Potential reduction of environmental impact

CO₂ emissions are also an important indicator in this study. Here, lower CO₂ emission from the heating systems, indicated more renewable energy. In general, 1 L of diesel oil can produce 2.640 kg-CO₂ and 1 kWh of electricity can produce 0.533 kg-CO₂. Therefore, the total CO₂ emission from a heating system was calculated and is shown in Table 14. For 1 year, the lowest CO₂ emission was from the SC-HP-37B-Systems because the heating capacity of the boiler was small; the highest CO₂ emission was from the HP-B-System because of high electricity use during the operating time.

4. Conclusion

The aim of this study was to reduce hypothermia damage in fisheries resulting from a cold stream on the basis of observations in a cold stream from January 22 to 26, 2016. The performance of an AF’s heating system and the temperature profile of the water body were investigated for 1 week: 3 normal days before a cold stream, 3 cold stream days, and 1 normal day after a cold stream. The aim of the heating system was to prevent the temperature of the water deviating from that required to sustain the living conditions of the farmed organisms, such as milkfish and whiteleg shrimp.

The physical model and government equations in STAR-CCM+ were validated in this study through comparisons of previous studies and experiments. After comparing different kinds of positions and

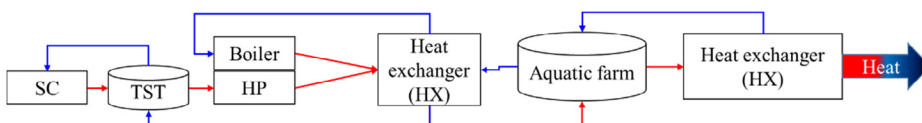


Fig. 16. Schematic of the layout of the TRNSYS of combined SC-HP-B-System.

Table 13

Parameter settings of combined SC-HP-B-System.

Parameters	Unit	Value
Solar collector (SC)		
Number in series	N/A	6
Collector area	m ²	230.4
Flow rate	kg/s	8
SC-temp difference controller		
Upper dead band dT	°C	7
Lower dead band dT	°C	3
Thermal storage tank (TST)		
Initial temperature	°C	24
Tank volume	m ³	20
Number of nodes	N/A	1
Tank loss coefficient	W/m ² -K	3

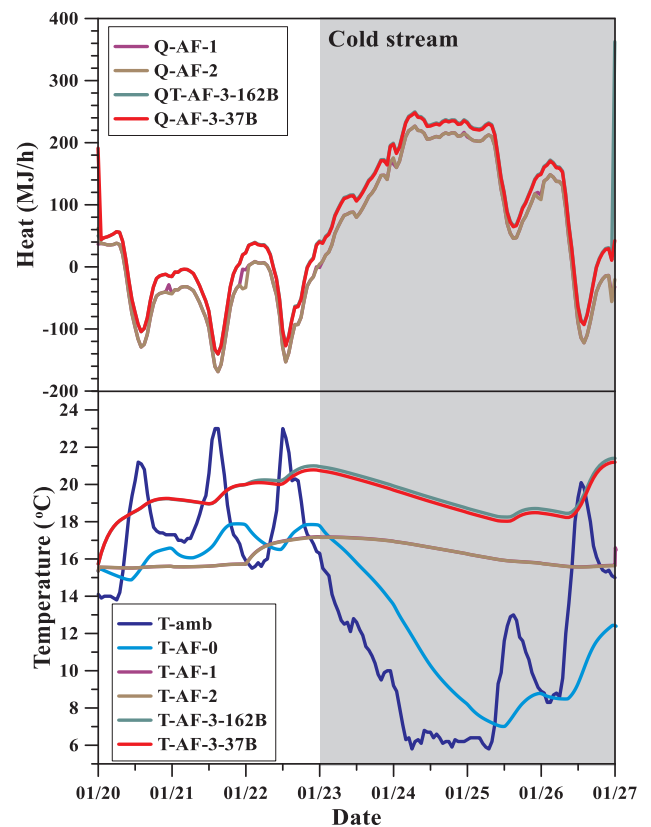


Fig. 17. AF temperature and heat loss of each heating system.

velocity of the inlets and positions of the outlets and setting the barriers in the AF, the optimized geometry—A3, B2, C2, and D3—was determined using the Taguchi method. The optimized geometry enhanced of the survival zone by 40% compared with the previous geometry.

Table 14
Heat gain and contributing proportion of heat system, cost, and CO₂ emissions of each heating system.

		B-System	HP-B-System	SC-HP-162B-Systems	SC-HP-37B-Systems
Total heat gain	(MJ)	1.250E+05	1.257E+05	1.276E+05	7.285E+04
Heat gain from each heating system					
Q _{SC}	(MJ)	0.000E+00	0.000E+00	1.888E+03	1.888E+03
Q _{HP}	(MJ)	0.000E+00	5.476E+04	5.476E+04	5.476E+04
Q _{Boiler}	(MJ)	1.250E+05	7.092E+04	7.092E+04	1.620E+04
Investment cost					
Solar collectors	(NTD)	0	0	1000 k	1000 k
20-tons TST	(NTD)	0	60 k	600 k	600 k
Heat pump	(NTD)	0	0	200 k	200 k
Circulating motor	(NTD)	0	10 k	10 k	10 k
Installation fee	(NTD)	0	200 k	200 k	200 k
Boiler	(NTD)	450 k	300 k	300 k	150 k
Operating cost					
Electricity	(kWh)	0.00	15151.20	4313.61	4313.61
Electricity fee	(NTD)	0.000	76.211 k	21.697 k	21.697 k
Diesel oil	(Liter)	3556.95	2005.81	2005.81	458.33
Diesel oil	(NTD)	95.326	53.756 k	53.756 k	12.283 k
Total cost	(NTD)	545.326	699.966 k	2385.453 k	2193.981 k
Assume NTD 155.263 k per 3-months; Assume one cold stream per year					
Payback period	(year)	4	5	15	14
CO ₂ emission from diesel oil					
CO ₂ emission	(kg)	9390.36	13370.92	7594.48	3509.15

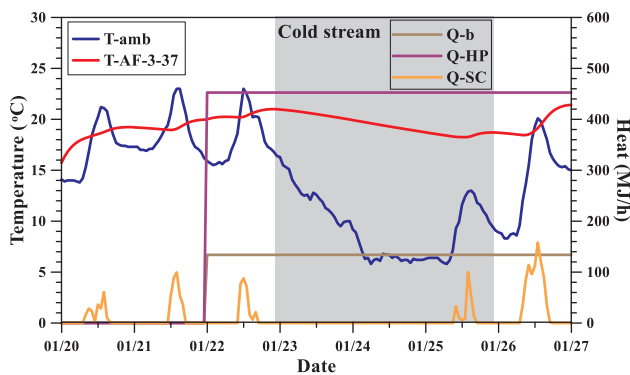


Fig. 18. Results of the SC-HP-B-System in a 37.2-kW heating-capacity boiler.

Therefore, this optimized geometry should be considered when establishing a circulatory system.

Here, TRNSYS model parameters were validated through comparisons in experiments. The HP-B-System, SC-HP-162B-System, and SC-HP-37B-System were unsuitable during the cold stream. The heat gain from the solar thermal was low during cloudy and rainy days, but the investment cost was high. The proportionate heat gain from the HP-B-System was 44% in HP and 56% in the boiler; the heat gain from the SC-HP-B-System in a 162.8-kW heating-capacity boiler was 56% in the boiler and 44% in the others. The reason for the proportion of the boiler being greater is related to the flow rate of the source side of the HX, which limits heat absorbcency. The heat gain from the SC-HP-B-System in a 37.2-kW heating-capacity boiler was 22% in the boiler and 78% in others. The heat gain from the HP was low because of the low ambient temperature and high relative humidity. When the temperature was low, the efficiency of the HPs was as low as the electric heater. Therefore, no purchase benefit was noted. From an environmental

Appendix A. Simulation model

The physical 3D models incorporate the parameter setting of unsteady state, gravity, and $k-\omega$ turbulence.

- Unsteady model

perspective, solar combisystems are effective in reducing CO₂ emissions, but the HPs are not as effective because the low environmental temperature causes the system efficiency to decrease to a level similar to that of an electric heater. Therefore, the boiler system remains the most effective during the cold stream, from both economic and environmental perspectives.

CRediT authorship contribution statement

Yueh-Heng Li: Conceptualization, Funding acquisition, Investigation, Methodology, Project administration, Resource, Supervision, Visualization, Writing - original draft, Writing - review & editing. **Yu-Ting Yang:** Data curation, Formal analysis, Software, Validation.

Declaration of Competing Interest

All authors declared that: (i) no support, financial or otherwise, has been received from any organization that may have an interest in the submitted work; and (ii) there are no other relationships or activities that could appear to have influenced the submitted work.

Acknowledgements

Computer time and numerical packages provided by Prof. Heiu-Jou Shaw (Department of Systems and Naval Mechatronic Engineering, National Cheng Kung University) and Prof. Keh-Chin Chang (Department of Aeronautics and Astronautics, National Cheng Kung University) are gratefully acknowledged. The authors thank the financial support from the Ministry of Science and Technology, Taiwan under the grant numbers, MOST 106-2923-E-006-003-MY3, MOST 106-3113-E-006-002-CC2, and MOST 108-2628-E-006-008-MY3.

This work aims to observe the effective volume of the survival zone after pouring hot water into the farm.

• Gravity

The presence of gravity is contingent on the impact of the buoyant force on thermal convection and flow dynamics. Moreover, the density of the working fluid is polynomial. Gravity should be taken into consideration.

In STAR-CCM+, it can count the effect of gravitational acceleration on materials in a physical continuum. For the fluids, it provides two effects. One is that the working pressure becomes the piezometric pressure (p_{piezo}), and the another is that the body force due to gravity is included in the momentum equations. In this study, the latter contributed more.

$$p_{piezo} = p_{static} - \rho_{ref} \hat{g} (\hat{x} - \hat{x}_0) \tag{1}$$

• Coupled flow and energy

The Coupled Flow model solves the conservation equations of mass, momentum, and energy simultaneously by using a pseudo-time-marching approach. The coupled flow and coupled energy models are best for natural convection problems. Because there are two attractive advantages; one is its robustness for solving flows with dominant source terms, and the another is that the convergence rate does not deteriorate as the mesh is refined.

• k- ω turbulence

A k- ω turbulence model is a two-equation model, as shown Eqns. 2 and 3 that solves transport equations for the turbulent kinetic energy and the specific dissipation rate. The most significant advantage is that it can be applied throughout the boundary layer, including the viscous-dominated region.

$$\frac{d}{dt} \int_V \rho k dV + \int_A \rho k (\hat{v} - \hat{v}_g) \cdot d\hat{a} = \int_A (\mu + \sigma_k \mu_t) \nabla k \cdot d\hat{a} + \int_V (\gamma_{trans} (G_k + G_{nl}) + G_k^{lim} - \gamma' \rho \beta^* f_{\beta^*} (\omega k - \omega_0 k_0) + S_k) dV \tag{2}$$

$$\frac{d}{dt} \int_V \rho \omega dV + \int_A \rho \omega (\hat{v} - \hat{v}_g) \cdot d\hat{a} = \int_A (\mu + \sigma_\omega \mu_t) \nabla \omega \cdot d\hat{a} + \frac{d}{dt} \int_V (G_\omega - \rho \beta (\omega^2 - \omega_0^2 k_0) + D_\omega + S_\omega) dV \tag{3}$$

where γ' is $\min[\max(\gamma_{trans}, 0.1), 1]$, S_k and S_ω are the user-specified source terms, k_0 and ω_0 are the ambient turbulence values in source terms that counteract turbulence decay and D_ω is a cross-derivative term. The production G_k is evaluated as with the standard k- ω model, as shown in Eq. (4). The production of ω is evaluated in Eqs. (5) and (6)

$$G_k = \mu_t f_c S^2 - \frac{2}{3} \rho k \nabla \cdot \hat{v} - \frac{2}{3} \mu_t (\nabla \cdot \hat{v})^2 \tag{4}$$

$$G_\omega = \rho \gamma \left[\left(S^2 - \frac{2}{3} (\nabla \cdot \hat{v})^2 \right) - \frac{2}{3} \omega \nabla \cdot \hat{v} \right] \tag{5}$$

$$\mu_t = \rho k T \tag{6}$$

Appendix B. Boundary conditions in simulation

Boundary	Boundary mode	Description
Inlets	Mass flow inlet	$\dot{m} = 25 \text{ kg/s}$; $I = 0.0411$; $\angle = 0.0406 \text{ m}$; $T = 20 \text{ }^\circ\text{C}$
Outlets	Flow-split outlet	Split ratio = 1
Floor	Wall	Constant temperature: $T = 10 \text{ }^\circ\text{C}$
Sidewalls	Wall	Table: Temperature change with depth
Surface	Wall	Ambient temperature = $6 \text{ }^\circ\text{C}$ Convection heat transfer = $10 \text{ W/m}^2\text{-K}$

References

[1] Y.-H. Li, H.-H. Chen, Analysis of syngas production rate in empty fruit bunch steam gasification with varying control factors, *Int. J. Hydrogen Energy* 43 (2018) 667–675.

[2] Y.-H. Li, H.-W. Hsu, Y.-S. Lien, Y.-C. Chao, Design of a novel hydrogen-syngas catalytic mesh combustor, *Int. J. Hydrogen Energy* 34 (2009) 8322–8328.

[3] Y.-H. Li, H.-T. Lin, K.-L. Xiao, J. Lasek, Combustion behavior of coal pellets blended with Miscanthus biochar, *Energy* 163 (2018) 180–190.

[4] Y.-M. Liu, K.-C. Chang, W.-M. Lin, K.-M. Chung, Solar thermal application for the livestock industry in Taiwan, *Case Stud. Therm. Eng.* 6 (2015) 251–257.

[5] K.-C. Chang, T.-S. Lee, W.-M. Lin, K.-M. Chung, Outlook for solar water heaters in Taiwan, *Energy Policy* 36 (2008) 66–72.

[6] J. Chu, C.A. Cruickshank, Solar-assisted heat pump systems: A review of existing studies and their applicability to the Canadian residential sector, *J. Sol. Energy Eng.* 136 (2014) 041013.

[7] G. Emmi, A. Zarrella, M. De Carli, A. Galgaro, An analysis of solar assisted ground source heat pumps in cold climates, *Energy Convers. Manage.* 106 (2015) 660–675.

[8] G. Panaras, E. Mathioulakis, V. Belessiotis, Investigation of the performance of a combined solar thermal heat pump hot water system, *Sol. Energy* 93 (2013) 169–182.

[9] W. Lerch, A. Heinz, R. Heimrath, Direct use of solar energy as heat source for a heat pump in comparison to a conventional parallel solar air heat pump system, *Energy Build.* 100 (2015) 34–42.

[10] D. Carbonell, M.Y. Haller, D. Philippen, E. Frank, Simulations of combined solar thermal and heat pump systems for domestic hot water and space heating, *Energy Procedia* 48 (2014) 524–534.

[11] D. Carbonell, M. Haller, E. Frank, Potential benefit of combining heat pumps with solar thermal for heating and domestic hot water preparation, *Energy Procedia* 57 (2014) 2656–2665.

[12] K. Kaci, M. Merzouk, N.K. Merzouk, M. El Ganaoui, S. Sami, R. Djedjig, Dynamic simulation of hybrid-solar water heated olympic swimming pool, *Energy Procedia* 139 (2017) 750–757.

- [13] T.T. Chow, Y. Bai, K.F. Fong, Z. Lin, Analysis of a solar assisted heat pump system for indoor swimming pool water and space heating, *Appl. Energy* 100 (2012) 309–317.
- [14] M. Dongellini, S. Falcioni, A. Martelli, G.L. Morini, Dynamic simulation of outdoor swimming pool solar heating, *Energy Procedia* 81 (2015) 1–10.
- [15] H.F. Nouanegue, S. Sansregret, B. Le Lostec, A. Daoud, Energy model validation of heated outdoor swimming pools in cold weather, *de Proceedings of Building Simulation*, 2011.
- [16] E. Hahne, R. Kubler, Monitoring and simulation of the thermal performance of solar heated outdoor swimming pools, *Sol. Energy* 53 (1994) 9–19.
- [17] E. Ruiz, P.J. Martínez, Analysis of an open-air swimming pool solar heating system by using an experimentally validated TRNSYS model, *Sol. Energy* 84 (2010) 116–123.
- [18] A. Cloteaux, F. Gerardin, N. Midoux, Numerical simulation and modelling of a typical swimming pool for disinfection by-products assessment, in: *4th International Pool and Spa Conference*, 2011.
- [19] L. Lewis, J. Chew, I. Woodley, J. Colbourne, K. Pond, The application of computational fluid dynamics and small-scale physical models to assess the effects of operational practices on the risk to public health within large indoor swimming pools, *J Water Health* 13 (2015) 939–952.
- [20] A. Cloteaux, F. Gérardin, N. Midoux, Influence of swimming pool design on hydraulic behavior: a numerical and experimental study, *Scientific Res.* 5 (2013) 14.
- [21] C.I. Roldan, S.D.R. Rico, Study of the homogenization of the water temperature in a heated pool under steady-state conditions to minimize the energy consumption of the heating system, *Energy Procedia* 57 (2014) 2879–2887.
- [22] W. Gao, T. Liu, W. Lin, C. Luo, Numerical study on mixing characteristics of hot water inside the storage tank of a solar system with different inlet velocities of the supply cold water, *Procedia Environ. Sci.* 11 (2011) 1153–1163.
- [23] M.R. Assari, H. Basirat Tabrizi, M. Savadkoohy, Numerical and experimental study of inlet-outlet locations effect in horizontal storage tank of solar water heater, *Sustainable Energy Technol. Assess.* 25 (2018) 181–190.
- [24] S. Ievers, W. Lin, Numerical simulation of three-dimensional flow dynamics in a hot water storage tank, *Appl. Energy* 86 (2009) 2604–2614.
- [25] Z. Lavan, J. Thompson, Experimental study of thermally stratified hot water storage tanks, *Sol. Energy* 19 (1977) 519–524.
- [26] L. Kenjo, C. Inard, D. Caccavelli, Experimental and numerical study of thermal stratification in a mantle tank of a solar domestic hot water system, *Appl. Therm. Eng.* 27 (2007) 1986–1995.
- [27] A.I. Stamou, Improving the hydraulic efficiency of water process tanks using CFD models, *Chem. Eng. Process. Process Intensif.* 47 (2008) 1179–1189.
- [28] J.P. Holman, *Heat transfer*, 1997.
- [29] J.-Y. Jeng, The cost-benefit analysis for the polyculture of milkfish (*Chanos chanos*) and white shrimp (*Litopenaeus vannamei*)—Kaohsiung County Mituo township as an example, in: *Department of Fisheries Production and Management*, Vol. Master, National Kaohsiung Marine University, 2009.